Journal Pre-proof

Nanofibrous glass/ceramic porous structures using high-temperature interface bonding

Andrei Stanishevsky (Conceptualization) (Methodology) (Data curation) (Supervision) (Writing - original draft), Courtney Severino (Methodology) (Visualization) (Investigation) (Writing - review and editing) (Data curation), Stacy Ross (Investigation) (Validation), Riley Yager (Investigation) (Writing - review and editing), Micah Armstrong (Visualization) (Investigation) (Writing - review and editing), Michał Binczarski (Investigation) (Data curation) (Software), Waldemar Maniukiewicz (Investigation) (Validation) (Methodology), Izabela Witońska (Investigation) (Validation) (Data curation)

PII: S2352-4928(21)00210-5

DOI: https://doi.org/10.1016/j.mtcomm.2021.102218

Reference: MTCOMM 102218

To appear in: *Materials Today Communications*

Received Date: 15 June 2020

Revised Date: 8 February 2021

Accepted Date: 25 February 2021

Please cite this article as: Stanishevsky A, Severino C, Ross S, Yager R, Armstrong M, Binczarski M, Maniukiewicz W, Witońska I, Nanofibrous glass/ceramic porous structures using high-temperature interface bonding, *Materials Today Communications* (2021), doi: https://doi.org/10.1016/j.mtcomm.2021.102218

Nanofibrous glass/ceramic porous structures using high-temperature interface bonding

Andrei Stanishevsky[1*], Courtney Severino[1], Stacy Ross[1], Riley Yager[1], Micah Armstrong[1], Michał Binczarski[2], Waldemar Maniukiewicz[2], Izabela Witońska[2]

[1]Department of Physics, University of Alabama at Birmingham, 1300 University Boulevard, Birmingham, AL 35294-1170, USA

[2]Institute of General and Ecological Chemistry, Faculty of Chemistry, Lodz University of Technology, Zeromskiego 116, 90-924 Lodz, Poland

*Corresponding author. Email: astan@uab.edu Tel: +205-934-8030

Highlights

- Nanofibrous silica glass/ceramic rigid 3-D shapes are fabricated for the first time
- Silica nanofibers with ceramic binder layer are stable up to 1200 °C
- Highly porous nanofibrous glass/ceramic can be stronger than microfibrous ceramics
- Fiber-binder layer interactions define the properties of glass-ceramic shapes

Abstract

Nanofibrous glass/ceramic rigid shapes with uncommon structures, consisting of electrospun vitreous silica nanofibers coated with 5–30 nm thick Al_2O_3 or $MgAl_2O_4$ ceramic layers, were fabricated in this study. Ceramic nanolayers restricted the viscous flow in silica nanofibers and provided strong structural bonding during partial sintering at 1200 °C. The interface interactions between the silica nanofiber core and ceramic nanolayer during sintering defined the resulting microarchitecture, porosity, and phase composition of the material. Nanofibrous glass-ceramic slabs with 90±2% porosity revealed flexural and compressive strengths in the range from 0.7 to

3.2 MPa due to the combined effects of the compounds formed in the silica nanofiber core, ceramic layer, and at their interface. The structural uniformity and mechanical properties of nanofibrous glass/ceramic shapes make them strong alternatives to microfibrous porous ceramics in various applications, especially when a small size of ceramic components is needed.

Keywords: Nanofibrous ceramic; Porous; Mechanical strength; Sintering.

1. Introduction

Fibrous ceramics represent a class of light-weight ceramic materials with typically high porosity up to 95%, low thermal conductivity, and high resistance to thermal shock [1–3]. These materials have been increasingly used in thermal insulation, aerogel/fibrous ceramic composites, catalyst supports, fuel cells, and various types of membranes and filters [4–6].

Fibrous ceramic materials are composed mainly of a random network of ceramic fibers and a high-temperature binder. Alumina, mullite, and zirconia fibers with diameters from a few to several tens of micrometers are commonly used. Fabrication process, sintering temperature, type and amount of binder play key roles in the formation of the microarchitecture and mechanical properties of fibrous ceramic shapes. For example, Cuo et al [6] fabricated filtration membranes from mullite fibers with 10–30 μm diameters and 100–200 μm lengths using a binder derived from kaolin-feldspar powder. The membranes revealed 78–74% porosity and 0.76–1.67 MPa compressive strength after sintering at 1250 °C. Fibrous mullite ceramic with ZrO_2-based binder [7–9] demonstrated the increase in compression strength from 0.6 MPa to 14 MPa when the porosity decreased from ~86 to 47%. It was observed that the decrease in porosity and increase in strength corresponded to a higher amount of binder (up to 70 wt%) in the material.

SiO_2-based binders have been, so far, the most frequently used in fibrous ceramic materials. Numerous reports [2,10–15] have shown that when silica sol is used, mullite fibrous ceramics with

different microarchitectures, 74–92% porosity, and 0.1–2.8 MPa compression strength can be fabricated after sintering at 1100–1500 ºC. Xu et al [16] noted that the binder can form either beads at the contact points between the fibers or continuous layers on the fiber surface. The latter led to a higher compressive strength of the resulting material. Mullite fibrous ceramics with silica binder derived from silicone resin [17,18] revealed 1.0–1.8 MPa compressive and 0.65–0.86 MPa flexural strength at 81–74 % porosity, depending on the sintering temperature (1200–1600 ºC). Zhang et al [19] prepared highly porous (86.2–89.2%) layered mullite-zirconia fibrous ceramic with a borosilicate binder by using unidirectional compression (80–240 kPa) of microfiber slurries in the mold. The compressive strength of the material varied in 2.42–5.74 MPa range, depending on the mullite/zirconia mass ratio, when the load was applied along the layers. However, the compressive strength was about 1.0 MPa when the load was applied normal to the layers. In most studies, depending on the fabrication procedure and precursors, the shrinkage of fibrous ceramic shapes in the range of 1.0–23 % and crystallization of silica binder to cristobalite were observed.

There has been an increasing effort to fabricate nanofibrous ceramic materials [20–24]. Such materials, made mainly by thermal processing of precursor fibers fabricated using electrospinning [25,26], have demonstrated promising results, but reports on nanofibrous ceramic shapes other than small area thin sheets or mats are scarce. For example, flexible nanofibrous ceramic sponges with extremely high porosity (>99%) have been fabricated using sol-gel casting and freeze-drying of oxide nanofiber slurries with a silica-based binder followed by sintering [27–29]. Such sponges demonstrated very low thermal conductivity, high compressibility and resilience under loads less than 20 kPa. The available data show that ceramic nanofibers can exhibit different mechanical properties than microfibers, which makes them an intriguing constituent for the development of advanced ceramic structures. Further research on ceramic nanofiber-based three-dimensional (3-

D) shapes with the range of porosities typical for fibrous ceramic is needed to explore the potential of nanofibrous ceramic materials.

This study has been focused on fabrication of rigid nanofibrous amorphous silica/ceramic highly porous structures with 3-D nanofiber packing, and an initial evaluation of their mechanical properties. The results have shown that by using vitreous silica nanofibers with a nanolayer of ceramic binder (Al_2O_3 or $MgAl_2O_4$), it is possible to form thermally stable (up to 1200 ºC) nanofibrous ceramic shapes with attractive microscale structural uniformity and mechanical properties. It has been determined that the ceramic nanolayer and its interaction with silica nanofibers during sintering can play critical roles in the formation of such nanofibrous silica-based glass-ceramic structures and their mechanical properties.

2. Experiment

2.1. Raw materials and precursors

Tetraethoxysilane (TEOS, 99%+), aluminum nitrate nonahydrate ($Al(NO_3)_3 \cdot 9H_2O$) and magnesium nitrate hexahydrate ($Mg(NO_3)_2 \cdot 6H_2O$), all supplied from Alfa Aesar, served as the sources for amorphous silica fibers and ceramic binder. Polyvinyl butyral (PVB, M_w ~70,000, 80% butyral, Scientific Polymer Products) was used as a carrier polymer for the silica nanofiber and ceramic binder precursor solutions. Hydrochloric acid (HCl) and ethanol (200 proof) were purchased from Fischer Scientific and Decon Labs, respectively. DI water was produced on site.

Silica nanofiber precursor was prepared from TEOS, ethanol, DI water, and HCl in 1.0/2.0/2.0/0.01 molar ratio according to the procedure described by Geltmeyer et al [30]. PVB solution in ethanol was added to the obtained silica sol to achieve the polymer concentration of 4.75±0.5 wt% in the precursor. The resulting silica/PVB precursor had apparent viscosity 110±10

mPa·s (at 1000 s^{-1} shear rate), electrical conductivity 170±30 μS/cm, and it was stable up to six months when stored at normal laboratory conditions at 21 °C and 42 % relative humidity.

Ceramic binder precursor stock solution was prepared by dissolving either $Al(NO_3)_3 \cdot 9H_2O$ (0.06 mol) or $Al(NO_3)_3 \cdot 9H_2O/Mg(NO_3)_2 \cdot 6H_2O$ (1:1 molar ratio, 0.03 mol of each) salts in 100 mL ethanol/H_2O (9:1 volume ratio) solvent that contained 1 wt% of PVB. Solutions with lower salts concentrations were prepared by diluting the stock solution with the same 1.0 wt% PVB/Ethanol/H_2O solvent.

2.2. Fabrication process for nanofibrous ceramic structures

Nanofibrous glass/ceramic porous shapes were fabricated using the procedure shown in Fig.1. First, the silica/PVB precursor fibers were produced by a high-yield alternating field electrospinning (AFES) process described elsewhere [31–33]. AFES is a free-surface electrospinning technique that generates dense, slowly moving (0.2–1.5 m/s) flows of propagating fibers that carry almost no electric charge. This process feature allows to use electrically non-conducting collectors and provides easy collection and handling of fibers [34]. AFES has been used for fabrication of sizeable quantities of SiO_2 [35], Al_2O_3 [36], ZrO_2 [37] and TiO_2 [38] nanofibers.

In present study, the silica/PVB precursor solution was supplied to the electrode held at 30–33 kV rms AC-voltage (Fig.1-a1,a2) and the generated liquid precursor jets solidified and deposited on a plastic collector to form up to 30×150 cm^2 fibrous sheets with the thickness up to 20 mm (Fig.1-b1). Fibrous silica/PVB sheets were cut into manageable pieces and calcined at 600 °C to form nanofibrous amorphous silica (Fig.1-b2) with 450±250 nm fiber diameters. Next, the nanofibrous silica sheets were chopped/grinded (Fig.1-b3,b4) to achieve the fiber length less than 40 μm, and the resulting fluffy silica nanofibrous material was placed into a beaker (Fig.1-c1). The

binder precursor solution with different salt concentrations was then added (Fig.1-c2) and the mixture was stirred and sonicated (Fig.1-c3) to form a silica nanofiber suspension with ~12.5±1.5 wt% loading of solid phase. The low viscosity binder solution did not affect the fiber dispersibility in the binder solution. The masses of salts used in the binder precursor solution were determined from the molar weight ratios of the salt and corresponding ceramic binder. The following formula was used to calculate the amounts of ceramic binder:

$$m_{\text{binder}} = (4 \cdot m_{\text{silica}} \cdot \rho_{\text{binder}} \cdot h)/(\rho_{\text{silica}} \cdot D) \qquad (1),$$

where m_{binder}, ρ_{binder} and m_{silica}, ρ_{binder} are the mass and specific gravity of ceramic binder (Al_2O_3 or $MgAl_2O_4$) and silica nanofibers, respectively, D is the average fiber diameter, and h is the binder layer thickness. The amounts of binder precursor were calculated to form approximately 5, 10, and 30 nm thick ceramic layers on the surface of silica nanofibers. These thicknesses of ceramic layers corresponded to 7.4/8.2, 13.8/15.2, and 32.4/34.9 wt% loading of Mg-spinel and alumina binder, respectively. The nanofiber suspension was poured into 25×6×3 mm^3 aluminum alloy molds, covered and dried at 40 ºC temperature (Fig.1-d1,d2,d3). Dry nanofibrous slabs were extracted from the molds, placed in a programmable furnace (KSL-1500X-S, MTI Corp., Richmond, CA, USA), where they were heated at 5 ºC/min, calcined at 800 ºC for 2h, and sintered at 1200 ºC for 2h (Fig.1-d4,d5). The resulting nanofibrous highly porous ceramic slabs (Fig.1-e1) were gently polished using sandpaper (600 grit) to reduce the surface non-uniformity (Fig.1-e2).

2.3. Characterization methods

The diameter, surface morphology, packing and interaction of fibers in nanofibrous slabs after the calcination and partial sintering were investigated by scanning electron microscopy with EDS detector (SEM/EDS, field-emission scanning electron microscope FEI Quanta 650). SEM imaging was performed in secondary electron mode, at an accelerating voltage 15–30 kV, electron probe

current 2 μA, and a chamber pressure of 1×10^{-4} Pa. EDS spectra were acquired using Bruker Flat Quad 5060F energy dispersive X-ray detector at an accelerating voltage 20 kV and electron probe current 5 μA. SEM samples were prepared by cleaving the nanofibrous slabs to study both their surface and internal microarchitecture. The samples were sputter coated with a few nm AuPd layer to reduce charging artifacts.

X-ray diffraction (XRD) patterns of nanofibrous glass/ceramic samples were obtained using an X'Pert Pro MPD diffractometer (PANalytical, the Bragg–Brentano geometry with Cu Kα tube operated at 40 kV and 45 mA and X'Celerator detector). Data were acquired over the range of 5–90° 2θ using the step of 0.0167° and dwelling time of 27 s. Samples were crushed, pressed into zero-background silicon holders, and rotated during the measurements to minimize the possibility of preferred orientation effects. Phase identification and crystallite size analysis were performed using the PANalytical High Score Plus software package and the International Centre for Diffraction Data (ICDD) powder diffraction file (PDF-2 ver. 2009) database.

Porosity of nanofibrous porous glass/ceramic slabs was evaluated from the formula

$$\varepsilon = (1 - \rho_{exp}/\rho_{dense})\times100\% \qquad (2)$$

where ρ_{exp} is the apparent density of the fibrous material, and ρ_{dense} is the density of the corresponding non-porous glass-ceramic fibers. The latter value was calculated using the known composition of fibers in terms of initial weight fractions of silica and ceramic (alumina or spinel binder, formula (1)) components, the crystalline phase composition determined by Rietveld analysis of XRD patterns, and the formula

$$\rho_{dense} = \sum X_i\rho_i/100 \qquad (3)$$

where X*i* are the mass% contributions of each identified phase (ρ_{silica} = 2.196 g/cm^3, ρ_{spinel} = 3.58 g/cm^3, $\rho_{alumina}$ = 3.98 g/cm^3, ρ_{crystb} = 2.33 g/cm^3, and ρ_{saph} = 3.49 g/cm^3 are the density of non-

porous amorphous silica, $MgAl_2O_4$ spinel, α-Al_2O_3, cristobalite and sapphirine, respectively). Specifically, in the case of partially sintered silica-spinel fibers, the comparison of Rietveld analysis data for cristobalite and ceramic phases with the initial mass ratio of silica and spinel helped to determine the relative amounts of the remaining amorphous silica in the fiber structure. Capillary flow PMI Simple Porometer with a custom measuring head for small nanofibrous slabs analysis and DI water as the wetting fluid was used to determine the pore size. At least three measurements were taken sequentially in dry and wet state for each tested sample. The contact angle of 0°, determined by PGX+ PocketGoniometer for all samples, was used in the calculation of pore size.

Compressive and flexural strengths of nanofibrous porous glass/ceramic slabs were determined using a custom-made micromechanical tester designed for fibrous ceramic materials and equipped with 1N and 25N DFG35 force gauges (Omega Engineering, Inc.) and motorized ThorLab MT1-Z8 precision stage. Each original slab was cut using a precision diamond saw into at least two pieces along its longest side and further trimmed to a typical size of 2.5×2.5×25 ±0.5 mm^3 for both types of the tests to follow the minimum size requirements set by ASTM C1161-18 and ASTM C1358-18 standards. The original slabs and samples with smaller dimensions have also been used for comparison. Compression and 3-point bending tests were performed at 0.005 mm/s displacement rate and data were corrected for the load cell and frame deflection, and initial position of the stage. The load-displacement datasets were used to build the stress-strain curves.

3. Results and Discussion

3.1.Microarchitecture development in fibrous SiO_2/ceramic system

The microarchitecture of fibrous slabs made of chopped, relatively short amorphous silica nanofibers without a ceramic binder represented a random fibrous network (Fig.2a) that was stable up to 1000 ºC without measurable changes in the slab's dimensions or shape. The binderless nanofibrous SiO_2 slabs sintered at 1000 ºC for 2 h revealed 93.9% total porosity and 0.134 g/cm^3 mass density. These slabs were strongly deformed and their volume reduced by ~92% after sintering at 1200 ºC. Although the fibrous nature of the material was still present after 2 h of sintering at 1200 ºC (Fg.2b), the diameter of fibers increased considerably as they fused and shrunk axially due to the viscous flow without undergoing the devitrification.

When ceramic binder was added, the shrinkage and change in the nanofibrous silica/ceramic slab's porosity after sintering at 1200 ºC strongly depended on the amount and composition of the binder (Fig. 3a). Even with 7.4/8.2 wt% of either $MgAl_2O_4$ or Al_2O_3 binder (~5 nm calculated layer thickness) the shrinkage was sharply reduced and nearly equal in all directions (Fig.3a and Table 1). Regardless the amount and type of binder, rather uniform nanofibrous glass-ceramic slab's microarchitectures were observed after sintering at 1200 ºC (Fig.3b,c). The evaluation of sample density uniformity has been made by cutting the samples in Fig.1 across the long side each 3 - 4 mm and determining the density of such small pieces (20–40 mm^3). The uniformity of samples mass density was found within 12 % of the average value for the entire sample.

The 1200 ºC sintered slabs had the porosity in the range from 88.5 to 91.5% with the mean pore size in the range from 4.1 to 5.3 μm, correspondingly, depending on the amount and composition of the binder. The maximum size of the pores did not exceed 20 and 35 μm for the slabs with 88.5 and 91.5% porosity, correspondingly. The fraction of the pores with the sizes larger than 10 mm was less than 10%, and the majority of pores (>60%) was less than 5.5 μm in all

structures. These pore sizes were calculated assuming circular or square pore cross-section and the actual pore size can be smaller because of the apparently various pore shapes as seen in Fig.3 [39].

Detailed SEM analysis of fabricated silica nanofiber-based glass/ceramic structures with different average thickness of ceramic nanolayer revealed that their porosity and morphological changes seemingly correlate with the extent of the nanofibrous slab's shrinkage (Fig.3a) and degree of fusion between the fibers (Fig.4). All samples after calcination at 800 °C (Fig.4a,e) showed that there was no binder material present as particles or aerogel between the silica nanofibers. It was assumed that the binder forms predominantly as a thin ceramic layer on the surface of fibers and on their bundles. The deformation of nanofiber shape observed after partial sintering at 1200 °C for 2 h can be the result of viscous flow in the silica core. However, the viscous flow is seemingly restricted by the presence of ceramic layer, and the alloying of fibers can occur primarily at the locations where such ceramic layer is incomplete or broken. In particular, the bundles or small aggregates of silica nanofibers may not be fully coated with the binder at the fiber contact points during the mixing stage (c2-c3 in Fig.1), which promoted the fiber alloying at those areas. Even slightly larger amounts of binder provide better fiber coverage and layer thickness, which lead to a less shrunk structure (Fig.4b-d and Fig.4f-h). The structures with $MgAl_2O_4$ spinel binder had clearly more interfiber fusion for each thickness of the binder layer. This can be due to the binder composition and its interaction with silica nanofibers. The spinel binder had noticeably stronger effect on the density, porosity, and shrinkage of such glass/ceramic fibrous material after sintering at 1200 °C (Table 1 and Fig.3a). Essentially the same microarchitectures were observed both at the surface and in the bulk of fibrous slabs with given amount and composition of the binder.

A closer look at the silica nanofibers with ceramic binder after calcination at 800 °C showed that the fiber surface morphology remained smooth (Fig.5a). Judging from a slight but visible SEM contrast difference between the SiO_2 fiber and binder materials, it was noted that single fibers and commonly observed two-to-five fiber bundles were almost completely coated with a binder layer (Fig.5a, regions II and III, respectively). It was difficult to locate the areas where the binder layer was damaged or incomplete (e.g., region I in Fig.5a). Individual silica nanofibers with ceramic nanolayer seem to maintain their shape after sintering at 1200 °C, whereas the fiber bundles fuse at the contact points and deform inside the ceramic layer (Fig. 5b,c). It was still problematic to locate the areas, except the broken fiber edges, where the ceramic layer was damaged (Fig.5d,e). Such locations helped to verify the ceramic binder layer thickness. For example, the thickness of Al_2O_3 binder layer in Fig.5e is close to expected 30 nm for this sample. However, the available data for that sample show the thickness variations from approximately 18 to 45 nm. It was not possible to determine the thickness of binder layer for samples with the projected 5 and 10 nm thicknesses of ceramic shell.

EDS analysis of sintered glass-ceramic structures confirmed their elemental compositions shown in Table 1, and relatively uniform binder coating of nanofibers. Yet, the local variations in the thickness of binder coating are expected due to the nanofiber bundling and presence of fibrous aggregates. Fig. 6 shows an example of SEM/EDS analysis of a segment of a silica twin-fiber bundle coated with Al_2O_3 binder layer. The EDS spectrum of this fiber (Fig.6e) shows less alumina than the whole sample (Fig.6f) due to a larger than average silica fiber diameter and partial delamination of the binder layer.

3.2. Crystalline phase analysis

The observed trends in the development of such nanofibrous glass/ceramic microarchitecture have been linked to the interaction of binder layer with silica nanofibers during sintering. Depending on the composition of the binder, XRD patterns of fibrous structures calcined at 800 ºC showed the formation of polycrystalline either γ-alumina (ICDD file 01-074-4629) and spinel (ICDD file #00-021-1152) layers with 8.0±0.3 and 11.7±0.3 nm crystallite size, respectively (Fig.7 and Fig.8). In the case of spinel (Fig.8, top), the peak intensities increased directly proportional to the binder layer thickness. Such correlation was much less pronounced in the case of alumina and it was associated with the presence of amorphous alumina phase (Fig.7, top) after calcination at 800 ºC. Sintering of silica/alumina fibrous structure at 1200 ºC led to crystallization of that amorphous component to a polycrystalline α-Al_2O_3 phase (ICDD file #01-073-6190) with 25.5±0.5 nm crystallite size (Fig.7, bottom). The peak intensities of γ-Al_2O_3 phase remained almost unchanged with respect to the intensity of broad silica peak after sintering at 1200 ºC, which can be the result of γ-Al_2O_3 stabilization by SiO_2 in a very thin layer on the fiber surface [40,41]. Using the expected average thicknesses of the alumina shell (5, 10 or 30 nm, depending on the sample composition) and the pattern refinement using Rietveld analysis, the amount of γ-Al_2O_3 phase corresponded to 4–6 nm thick metastable layer which, most probably, creates an interface between the silica nanofiber and α-Al_2O_3 layer. Therefore, γ-Al_2O_3 was retained as the main phase in the fibers with the thinnest (~5 nm) alumina layer. A characteristic broad peak of amorphous silica shifted in this case from 2θ≈22.5º (800 ºC) to 2θ≈21.5º (1200 ºC) due to structural rearrangement in a cristobalite-like structure of a SiO_2 cluster network [42].

The presence of Mg-ions in nanofibrous silica/spinel structure stimulated the devitrification of amorphous silica and crystallization of cristobalite (ICDD file #01-077-1317) with 16.6±0.4 crystallite size during sintering at 1200 ºC for 2 h (Fig.8, bottom) [43]. The crystallization was not

complete and some amorphous silica was still present. The formation of cristobalite can also contribute, due to its higher density, to the shrinkage of silica fibers. The formation of at least one additional crystalline phase with 21.9±0.3 nm crystallite size, identified as sapphirine (magnesium aluminum silicate, $Mg_{3.5}Al_9Si_{1.5}O_{20}$ monoclinic phase, ICDD file #00-021-0549) was also observed [44]. The polycrystalline $MgAl_2O_4$ spinel phase with 16.0±0.4 nm crystallite size was still present, and the content of sapphirine phase was about 25 mol% of the spinel phase. It has been suggested that, unlike in the case of Al_2O_3 layer, a rather broad, mixed phase diffusion ceramic interlayer forms between the initial spinel binder layer and silica fibers. As the result, it was not possible to determine the actual thickness of such layer after sintering at 1200 ºC.

The differences in the sintering behavior of these nanofibrous systems at 1200 ºC led to the suggestion that both alumina and Mg-spinel form ceramic layers that restrict the silica viscous flow and help to preserve the fibrous microarchitecture and high porosity of the original silica nanofiber network. The presence of silica nanofiber bundles (Fig.5a-c) and, therefore, a larger number of contact points between the fibers not coated with ceramic layer, can be primarily responsible for the fiber alloying and structure shrinkage, especially with thinner layers (e.g., 5 nm). In the case of spinel layer, the diffusion of Mg atoms can also reduce the viscosity of silica [45], which could result in faster shrinkage before the viscous flow in silica core fiber was inhibited by the crystallization of cristobalite and sapphirine nanocrystalline phases. These competing processes seem to be strongly affected by the thickness of spinel binder layer (the source of Mg). Assuming that the relative amount of spinel phase in ceramic layer of different thickness remains about the same during sintering, the devitrification of silica and formation of cristobalite phase seem to occur faster when the spinel layer thickness increases. This can explain a sharper change

in the shrinkage of nanofibrous silica/spinel structure and its lesser magnitude than for silica/alumina at the same 30-nm ceramic layer thickness (Fig.3a).

Both alumina and spinel layers themselves do not seem to contribute to the observed crystallization behavior and shrinkage of nanofibrous silica/ceramic structure. The alumina and Mg-spinel nanofibers prepared independently by the same method [36] showed slightly larger crystallite size and little fusion between the fibers at the same sintering conditions.

3.3.Mechanical Properties

Preliminary tests of the mechanical properties of both types of nanofibrous glass/ceramic structures sintered at 1200 ºC indicated similar porosity-dependent stress-strain behavior (Fig.9a,b) as well as the trends in compressive and flexural strength (Fig.10a,b) after calcination at 800 ºC and partial sintering at 1200 ºC. Such similarity is frequently observed for cellular ceramics [46], in part, due to bending dominated behavior of open cell structures under compression [47,48]. On average, fibrous silica/spinel slab structures calcined at 800 ºC showed higher magnitudes of strength (0.4–1.1 MPa) in both bending and compression than silica-alumina structures (0.2–0.6 MPa) with similar porosities (Fig.10a,b). This can occur because the binder layer worked as an adhesive at the fiber intercept points. For comparison, nanofibrous SiO_2 slabs prepared without a binder at that temperature showed only ~0.07 MPa strength in both bending and compression. The difference in the mechanical strength of silica/alumina and silica/spinel samples with almost the same porosity can be associated with the formation of fully crystallized Mg-spinel nanolayer, whereas alumina layer was still mainly amorphous with significantly lower strength then crystalline alumina [49]. The observed strength numbers are comparable with some ceramic materials of similar porosity, which are made of ceramic microfibers with silica binder

but sintered at higher temperatures (Table 2). Nanofibrous silica with both alumina and spinel ceramic binder revealed 1.5–3.2 MPa compression and 0.7–2.7 MPa flexural strengths after partial sintering at 1200 °C. These strength numbers are noticeably higher than those reported for the most of ceramic microfiber-based ceramics with similar porosities (Table 2). There was little effect of the nanofibrous test specimen size on its mechanical properties observed. The mechanical behavior of nanofibrous slabs was primarily related to their cellular microarchitecture with the cell size roughly corresponding to mean pore size (4.1–5.3 μm). Both flexural and compressive strengths show a trend to increase with decreasing porosity of silica/alumina samples. However, there are relatively small changes in strength values for silica/spinel samples with porosities in 88.5–91.5% range. The latter result can be explained by the presence of a larger fraction of ceramic component in samples with lower density (Table 1), which contributed to their increased strength at higher porosity. The density of silica/alumina fibrous slabs did not change gradually with the increase of ceramic fraction and degree of shrinkage. As a result, the samples with the 30-nm ceramic layer (largest amount of ceramic fraction) had the lowest porosity, whereas the samples with 10-nm ceramic layer had the highest porosity, and the samples with 5-nm ceramic layer (~89.9% porosity) were between. The combined effect of phase composition, porosity, and binder layer thickness led to some deviation of the observed strength-porosity relationships (Fig.10a,b) from commonly used power law for porous and cellular materials [46-48]:

$$\sigma^*/\sigma_{dense} = C\times(\rho^*/\rho_{dense})^n, \qquad (4)$$

where σ^*, ρ^* and σ_{dense}, ρ_{dense} are the strength and density for porous and dense states of the material, respectively, and C is the dimensionless constant, frequently selected as 1.0, and n varies depending on the cell geometry (e.g., n=2 and n=3 for open and closed cell structure, respectively). The compressive strength data for nanofibrous glass/ceramic slab structures fit between the

theoretical curves for pure silica at n=2 and n=3 (Fig.10b). Overall, the results for both silica/alumina and silica/spinel fibrous slabs follow relatively closely the trend described by the function (5)

$$\sigma^*/\sigma_{\text{dense}} = 0.3\times(\rho^*/\rho_{\text{dense}})^{2.2}, \qquad (5)$$

which can be due to the relatively close magnitudes of compressive strengths reported for silica, Mg-spinel, and alumina, and cell shape and cell wall (strut) thickness. Flexural strength of sintered nanofibrous slabs can be described by relationship (4) at n≈1.5 and C=0.8 if the flexural strength of dense silica (~60 MPa) is used in calculation (Fig.10a). Similar n and C parameters, characteristic for the bending-dominated behavior of open-cell structure [47,48], were determined for the dependence of tensile strength on porosity of the compressed nanofibrous vitreous silica thin meshes [35]. However, the flexural strength of nanofibrous glass/ceramic slab structure also fits the relationship (4) at n = 2.5÷2.8 if much higher strength of dense composite glass/ceramic material (450–800 MPa) is considered due to the presence of ceramic shell of different thickness (Table 1). The latter statement seems realistic and it indicates that the ceramic binder layer can results in a significant increase in the flexural strength of nanofibrous silica glass/ceramic structure. The highest strength values, 2.2–2.7 MPa (bending) and 2.6–2.9 MPa (compression) were achieved for silica/alumina slabs with 88.5% porosity and ~30-nm ceramic layer. Such close strength values, including a case when flexural strength exceeded compressive strength at plateau (Fig.10b) in one sample, occurred because of bending dominated behavior in tested structures and possible edge effects due to small sample size, nonuniform loading, and accumulating damage due to multiple struts failure [46-48]. These effects can also lead to the underestimated compressive strength when porosity decreases.

4. Conclusions

Nanofibrous vitreous silica-based glass/ceramic rigid shapes with 88–92% porosity, uncommon microarchitecture, thermal stability, good mechanical integrity and strength have been fabricated by a simple pressureless molding technique from electrospun silica nanofibers by using high-temperature nanocrystalline Al_2O_3 and $MgAl_2O_4$ ceramic binders. Small fiber diameter helps to achieve uniform mixing of the precursor components and the formation of homogeneous nanofibrous ceramic 3-D structure at microscale. The interaction between the silica nanofiber core and ceramic nanolayer (either alumina or Mg-spinel) during sintering determined the development of the resulting SiO_2 nanofiber core/ceramic layer microarchitecture. The mechanical behavior of fabricated nanofibrous glass-ceramic structures is determined by a combined effect of their structural components at given porosity. Flexural and compressive strengths of nanofibrous shapes sintered at 1200 ºC can be apparently higher than those reported for microfibrous ceramic materials with comparable porosities and sintered at higher temperatures with a silica-based binder. It is expected that a better dispersion of ceramic nanofibers in the binder precursor solution can further increase the material uniformity and mechanical strength. More research is necessary to investigate the role of nanofiber diameter, length, and composition on the sintering process and properties of fabricated nanofibrous structures with larger dimensions and shapes commonly used in tests and practical applications. It is anticipated that the nanofibrous glass/ceramic, as well as other nanofibrous ceramic/ceramic materials can offer appealing structural uniformity and properties, which make them viable alternatives to microfibrous ceramics in different applications, especially when a small size of ceramic components is needed.

Acknowledgements

This work has been primarily supported by the National Science Foundation (NSF) [Grant number DMR-1708600]. CS, RY and MA thank the support from the NSF International Research Experience for Students (IRES) Program [Grant number OISE-1558268].

Declaration of competing interest

The authors declare that they have no known competing financial interests or personal relationships that could have appeared to influence the work reported in this paper.

CRediT authorship contribution statement

Andrei Stanishevsky: Conceptualization, Methodology, Data curation, Supervision, Writing - original draft. Courtney Severino: Methodology, Visualization, Investigation, Writing – review & editing, Data curation. Stacy Ross: Investigation, Validation. Riley Yager: Investigation, Writing – review & editing. Micah Armstrong: Visualization, Investigation, Writing – review & editing. Michał Binczarski: Investigation, Data curation, Software. Waldemar Maniukiewicz: Investigation, Validation, Methodology. Izabela Witońska: Investigation, Validation, Data curation.

References

[1] J. Sun, Z. Hu, J. Li, H. Zhang, C. Sun, Thermal and mechanical properties of fibrous zirconia ceramics with ultra-high porosity, Ceram. Int. 40 (2014) 11787–11793. https://doi.org/10.1016/j.ceramint.2014.04.008

[2] J. He, X. Li, D. Su, H. Ji, X. Wang, Ultra-low thermal conductivity and high strength of aerogels/fibrous ceramic composites, J. Eur. Ceram. Soc. 36 (2016) 1487–1493. https://doi.org/10.1016/j.jeurceramsoc.2015.11.021

[3] J. Zhang, X. Dong, F. Hou, H. Du, J. Liu, A. Guo, Effects of fiber length and solid loading on the properties of lightweight elastic mullite fibrous ceramics, Ceram. Int. 42 (2016) 5018–5023. https://doi.org/10.1016/j.ceramint.2015.11.176

[4] R. Zhang, X. Ho, C. Ye, B. Wang, Enhanced mechanical and thermal properties of anisotropic fibrous porous mullite/zirconia composites produced using sol-gel impregnation, J. Alloys Compound. 699 (2017) 511–516. http://dx.doi.org/10.1016/j.jallcom.2017.01.007

[5] Y. Yu, K. Peng, J. Fang, R. Zhang, G. Wang, X. Peng, Mechanical and thermal conductive properties of fiber-reinforced silica-alumina aerogels, Int. J . Appl. Ceram. Technol. 15 (2018) 1138–1145. http://dx.doi.org/10.1111/ijac.12891

[6] Z. Cuo, H. Liu, F. Zhao, W. Li, S. Peng, Y. Chen, Highly porous fibrous mullite ceramic membrane with interconnected pores for high performance dust removal, Ceram. Int. 44 (2018) 11778–11782. https://doi.org/10.1016/j.ceramint.2018.03.259

[7] X. Hou, Z. Liu, Z. Liu, L. Yuan, J. Yu, Porous fibrous ZrO_2-mullite ceramics prepared via tert-butyl alcohol-based gel-casting, Ceram. Int. 44 (2018) 13580–13587. https://doi.org/10.1016/j.ceramint.2018.04.192

[8] M. Yang, X. Luo, J. Yi, M. Yu, X. Zhang, A novel way to fabricate fibrous mullite ceramic using sol-gel vacuum impregnation, Ceram. Int. 44 (2018) 12664–12669. https://doi.org/10.1016/j.ceramint.2018.04.066

[9] L. Yuan, Z. Liu, X. Hou, Z. Liu, Q. Zhu, S. Wang, B. Ma, J. Yu, Fibrous ZrO_2 -mullite porous ceramics fabricated by a hydratable alumina based aqueous gel-casting process, Ceram. Int. 45 (2019) 8824–8831. https://doi.org/10.1016/j.ceramint.2019.01.209

[10] T. Jia, H. Chen, X. Dong, W. Zang, A. Guo, J. Liu, Preparation of homogeneous mullite fibrous porous ceramics consolidated by propylene oxide, Ceram. Int. 45 (2019) 2474–2482. https://doi.org/10.1016/j.ceramint.2018.10.174

[11] D. Zhang, L. Li, X. Chen, L. Yang, X. Hu, A. Guo, D. Xie, W. Wang, H. Du, Fabrication of mullite fiber porous ceramics with even structures by filtration freeze-drying , J. Ceram. Soc. Jpn. 127 (2019) 5–10. https://doi.org/10.2109/jcersj2.18117

[12] J. Zhang, X. Dong, F. Hou, H. Du, J. Liu, A. Guo, Effects of fiber length and solid loading on the properties of lightweight elastic mullite fibrous ceramics, Ceram. Int. 42 (2016) 5018–5023.

https://doi.org/10.1016/j.ceramint.2015.11.176

[13] D. Liu, P. Hu, G. Zhao, W. Han, Silica bonded mullite fiber composite with isotropic geometry and properties for thermal insulating, J. Alloys Compound. 728 (2017) 1049–1057. https://doi.org/10.1016/j.jallcom.2017.08.140

[14] W. Zang, F. Guo, J. Liu, H. Du, F. Hou, A. Guo, Lightweight alumina based fibrous ceramics with different high temperature binder, Ceram. Int. 42 (2016) 10310–10316

http://dx.doi.org/10.1016/j.ceramint.2016.03.170

[15] W. Zang, T. Jia, X. Dong, J. Liu, H. Du, F. Hou, A. Guo, Preparation of homogeneous mullite-based fibrous ceramics by starch consolidation, J. Am. Ceram. Soc. 101 (2018) 3138–3147. https://doi.org/10.1111/jace.15441

[16] X. Xu, X. Dong, A. Guo, M. Wang, G. Sui, J. Liu, Effect of binder types on the properties of the mullite fibrous ceramics prepared by TBA-based gel-casting method, Ceram. Int. 43 (2017) 228–233. https://doi.org/10.1016/j.ceramint.2016.09.143

[17] X. Dong, G. Sui, Z. Yun, M. Wang, A. Guo, J. Zhang, J. Liu, Effect of temperature on the mechanical behavior of mullite fibrous ceramics with a 3D skeleton structure prepared by molding method, Mater. Design, 90 (2016) 942–948. https://doi.org/10.1016/j.matdes.2015.11.043

[18] W. Zhu, A. Guo, Y. Xue, J. Zhang, Z. Liu, C. Cao, F. Zhang, J. Liu, Mechanical evaluations of mullite fibrous ceramics processed by filtration and in situ pyrolysis of organic precursor, J. Eur. Ceram. Soc. 39 (2019) 1329–1335. https://doi.org/10.1016/j.jeurceramsoc.2018.11.024

[19] R. Zhang, X. Hou, C. Ye, B. Wang, D. Fang, Fabrication and properties of fibrous porous mullite–zirconia fiber networks with a quasi-layered structure, J. Eur. Ceram. Soc. 36 (2016) 3539–3544. http://dx.doi.org/10.1016/j.jeurceramsoc.2016.06.003

[20] A. La Monaca, A. Paolella, A. Guerfi, F. Rosei, K. Zaghib, Electrospun ceramic nanofibers as 1D solid electrolytes for lithium batteries, Electrochem. Comm. 104 (2019) Art.ID 106483. http://dx.doi.org/10.1016/j.elecom.2019.106483

[21] S.T. Aruna, L.S. Balaji, S.S. Kumar, B.S. Prakash, Electrospinning in solid oxide fuel cells – A review, Renew. Sust. Energ. Rev. 67 (2017) 673–682. https://doi.org/10.1016/j.rser.2016.09.003

[22] Y. Dai, W. Liu, E. Formo, Y. Sun, Y. Xia, Ceramic nanofibers fabricated by electrospinning and their applications in catalysis, environmental science, and energy technology, Polym. Adv. Technol. 22 (2011) 326–338. https://doi.org/10.1002/pat.1839

[23] H. Wu, W. Pan, D. Lin, H. Li, Electrospinning of ceramic nanofibers: Fabrication, assembly and applications, J. Adv. Ceram. 1 (2012) 2–23. https://doi.org/10.1007/s40145-012-0002-4

[24] W. Fu, Y. Dai, J. Tian, C. Huang, Z. Liu, K. Liu, L. Yin, F. Huang, Y. Lu, Y. Sun, In situ growth of hierarchical Al_2O_3 nanostructures onto TiO_2 nanofibers surface: Super-hydrophilicity, efficient oil/water separation and dye-removal, Nanotechnol. 29 (2018) Art.ID 345607. https://doi.org/10.1088/1361-6528/aac9ab

[25] K. Garg, G.L. Bowlin, Electrospinning jets and nanofibrous structures, Biomicrofluidics **5** (2011) Art.ID 013403.

[26] H. Niu, T. Lin, Fiber generators in needleless electrospinning, J. Nanomat. 2012 (2012) Art.ID 725950. https://doi.org/10.1063/1.3567097

[27] R. Liu, X. Dong, S. Xie, T. Jia, Y. Xue, J. Liu, W. Jing, A. Guo, Ultralight, thermal insulating, and high-temperature-resistant mullite-based nanofibrous aerogels, Chem. Eng. J. 360 (2019) 464–472. https://doi.org/10.1016/j.cej.2018.12.018

[28] L. Dou, X. Zhang, X. Cheng, Z. Ma, X. Wang, Y. Si, J. Yu, B. Ding, Hierarchical Cellular Structured Ceramic Nanofibrous Aerogels with Temperature-Invariant Superelasticity for Thermal Insulation, ACS Appl. Mater. Interf. 11 (2019) 29056–29064 https://doi.org/10.1021/acsami.9b10018

[29] H. Wang, X. Zhang, N. Wang, Y. Li, X. Feng, Y. Huang, C. Zhao, Z. Liu, M. Fang, G. Ou, H. Gao, X. Li, H. Wu, Ultralight, scalable, and high-temperature–resilient ceramic nanofiber sponges, Sci. Adv. 3 (2017) Art.ID e1603170, https://doi.org/10.1126/sciadv.1603170

[30] J. Geltmeyer, J. De Roo, F. Van den Broeck, J.C. Martins, K. De Buysser, K. De Clerck, The influence of tetraethoxysilane sol preparation on the electrospinning of silica nanofibers, J. Sol-Gel Sci. Technol. 77 (2016) 453–462. https://doi.org/10.1007/s10971-015-3875-1

[31] P. Pokorny, E. Koštáková, F. Sanetmik,P. Mikes, J. Chvojka, T. Kalous, M. Bilek, K. Pejchar, J. Valtera, D. Lukaš, Effective AC needleless and collectorless electrospinning for yarn production, Phys. Chem. Chem. Phys.16 (2014) 26816–26822. https://doi.org/10.1039/c4cp04346d

[32] C. Lawson, A. Stanishevsky, M. Sivan, P. Pokorny, D. Lukáš, Rapid fabrication of poly(ε-caprolactone) fibers using needleless alternating current electrospinning, J. Appl. Polym. Sci. 133 (2016) Art.ID 43232. https://doi.org/10.1002/app.43232

[33] K. Paulett, W.A. Brayer, K. Hatch, T. Kalous, J. Sewell, T. Liavitskaya, S. Vyazovkin, F. Liu, D. Lukáš, A. Stanishevsky, Effect of nanocrystalline cellulose addition on needleless alternating current electrospinning and properties of nanofibrous polyacrylonitrile meshes, J. Appl. Polym. Sci. 135 (2018) Ar.ID 45772. https://doi.org/10.1002/app.45772

[34] J. Valtera, T. Kalous, P. Pokorny, O. Batka, M. Bilek, J. Chvojka, P. Mikes, E. Kuzelova Kostakova, J. Spankova, J. Beran, A. Stanishevsky, D. Lukas, Fabrication of dual-functional composite yarns with a nanofibrous envelope using high throughput AC needleless and collectorless electrospinning, Sci. Rep. 9, (2019) Art.ID 1801 https://doi.org/10.1038/s41598-019-38557-z

[35] A. Stanishevsky, J. Tchernov, Mechanical and transport properties of fibrous amorphous silica meshes and membranes fabricated from compressed electrospun precursor fibers, J. Non-Cryst. Sol. 525 (2019) Art.ID 119653.https://doi.org/10.1016/j.jnoncrysol.2019.119653

[36] A. Stanishevsky, W.A. Brayer, P. Pokorny, T. Kalous, D. Lukáš, Nanofibrous alumina structures fabricated using high-yield alternating current electrospinning, Ceram. Int. 42 (2016) 17154–17161. https://doi.org/10.1016/j.ceramint.2016.08.003

[37] A. Stanishevsky, R. Yager, J. Tomaszewska, M. Binczarski, W. Maniukiewicz, I. Witońska, D. Lukas, Structure and mechanical properties of nanofibrous ZrO_2 derived from alternating field electrospun precursors, Ceram. Int. 45 (2019) 18672–18682. https://doi.org/10.1016/j.ceramint.2019.06.092

[38] S.L. Nealy, C. Severino, W.A. Brayer, A. Stanishevsky, Nanofibrous TiO_2 produced using alternating field electrospinning of titanium alkoxide precursors: crystallization and phase development, RSC Adv. 10 (2020) 6840–6849. https://doi.org/10.1039/c9ra10464j

[39] A. Jena, K. Gupta, Liquid Extrusion Techniques for Pore Structure Evaluation of Nonwovens, Int. Nonwovens J. 12 (2003) 45 – 53. https://doi.org/10.1177/1558925003os-1200313

[40] F. Nahif, D. Music, S. Mráz, M. To Baben, J.M. Schneider, Ab initio study of the effect of Si on the phase stability and electronic structure of γ- and α-Al_2O_3, J. Phys. Cond. Matt. 25 (2013) Art. ID 125502. https://doi.org/10.1088/0953-8984/25/12/125502

[41] M.K. Mardkhe, B. Huang, C.H. Bartholomew, T.M. Alam, B.F. Woodfield, Synthesis and characterization of silica doped alumina catalyst support with superior thermal stability and unique pore properties, J. Porous Mater. 23 (2016) 475–487. https://doi.org/10.1007/s10934-015-0101-z

[42] J.R. Martínez, S. Palomares-Sánchez, G. Ortega-Zarzosa, F. Ruiz, Y. Chumakov, Rietveld refinement of amorphous SiO_2 prepared via sol–gel method, Mater. Lett. 60 (2006) 3526–3529. https://doi.org/10.1016/j.matlet.2006.03.044

[43] I. Zaplatynsky, Effect of Al_2O_3, CaO, Cr_2O_3, and MgO on devitrification of silica, NASA Technical Memorandum, 101335 (1998) 14 p.

[44] C.C. Lin, A. Zangvil, R. Ruh, Phase Evolution in Silicon Carbide–Whisker-Reinforced Mullite/Zirconia Composite during Long-Term Oxidation at 1000° to 1350°C, J. Am. Ceram. Soc. 83 (2000) 1797–803. https://doi.org/10.1111/j.1151-2916.2000.tb01466.x

[45] M.I. Ojovan, Viscosity and glass transition in amorphous oxides, Adv. Condens. Matt. Phys. 2008 (2008) Art. ID 817829. https://doi.org/10.1155/2008/817829

[46] L.J. Gibson, M.F. Ashby, Cellular solids: structure and properties, Second ed., Cambridge University Press, Cambridge, UK, 1997.

[47] R. Brezny, D.J. Green, Mechanical Behavior of Cellular Ceramics, in: Materials Science and Technology, V.9, WILEY-VCH Verlag GmbH & Co KGaA, 2006, pp. 465 - 516. https://doi.org/10.1002/9783527603978.mst0125

[48] M.F. Ashby, Cellular Solids – Scaling of Properties, in: M. Scheffler, P. Colombo (Eds.), Cellular Ceramics: Structure, Manufacturing, Properties and Applications, WILEY-VCH Weinheim, 2005, pp. 3–17.

[49] G. Alcala, P. Skeldon, G.E. Thompson, A.B. Mann, H. Habazaki, K. Shimizu, Mechanical properties of amorphous anodic alumina and tantala films using nanoindentation, Nanotechnol. 13 (2002) 451-455. https://doi.org/10.1088/0957-4484/13/4/302

Table 1. Density and shrinkage of nanofibrous glass/ceramic structures after the calcination and sintering at 800 and 1200 ºC, respectively. Shrinkage data are shown for the temperature range from 800 to 1200 ºC.

Composition	Specimen	Binder, wt%	Density, g/cm^3, 800 ºC	Density, g/cm^3, 1200 ºC	Volume shrinkage, %	Linear shrinkage, %
SiO_2/Al_2O_3 5-nm layer	AlO-5	8.2	0.160	0.208	23.0	8.4
SiO_2/Al_2O_3 10-nm layer	AlO-10	15.2	0.165	0.194	15.0	5.3
SiO_2/Al_2O_3 30-nm layer	AlO-30	34.9	0.187	0.216	13.4	4.7
$SiO_2/MgAl_2O_4$ 5-nm layer	Sp-5	7.4	0.154	0.261	41.0	16.1
$SiO_2/MgAl_2O_4$ 10-nm layer	Sp-10	13.8	0.186	0.219	15.1	5.3
$SiO_2/MgAl_2O_4$ 30-nm layer	Sp-30	32.4	0.203	0.214	5.2	1.7

Table 2. Strength of nanofibrous glass/ceramic structures *vs* fibrous ceramic materials with similar porosities.

Composition of fiber core/binder	Fiber diameter, μm	Temperature, ºC	Porosity, %	Strength, MPa	Ref.
Silica/Al_2O_3 or $MgAl_2O_4$	0.3–0.8	1200	88.5– 91.7	1.5–3.2 (compres.) 0.7–2.7 (flexural)	Present work
Mullite/silica	0.3–0.6	1200–1400	99	0.015–0.019	[27]
Al_2O_3/Silica	5–10	1300–1500	88–92	0.1–0.6	[14]
Mullite/silica	10–20	1250	74–78	0.76–1.67	[6]
Mullite/silica	3–5	1500	74–79	0.73–1.72	[10]
Mullite/silica	10	1300	88.5	1.3	[11]
Mullite/silica	10–20	1400	84–90	0.5–1.2	[13]
Mullite/Silica	3–5	1500	80–85	0.3–0.8	[15]
Mullite/silica	10–15	1300–1500	81–82	1.21–1.58 (compres.) 0.65–0.7 (flexural)	[17]
Mullite/silica	10–15	1200–1500	74–81	1.4–1.8	[18]
Mullite/ borosilicate glass	10–15	1500	82.1– 86.4	0.93–1.46	[16]
Mullite/borosilicate glass	3–5	1450	87–91.8	0.68–1.97 (z) 2.42–5.74 (x-y)	[19]
Mullite -ZrO_2 /Al_2O_3-SiO_2	3–7	1400	78.1	1–1.4	[4]
Mullite/SiO_2-ZrO_2	10–15	1200	85	1.3	[2]
Mullite/ZrO_2	15–20	1600	84	0.54	[7]
Mullite/ZrO_2	5	1550	86.4	0.62	[8]

Figure Captions

Figure 1. Fabrication process of nanofibrous glass/ceramic porous structures: (a1, a2) Silica/PVB fibers are produced by AFES process and collected (b1) to form large fibrous sheets; (b2) As-spun sheets are cut and calcined at 600 ºC to form nanofibrous amorphous silica; (b3,b4) Calcined material is chopped/grinded and (c1) placed into a beaker; (c2) Binder precursor solution is added; (c3) The mixture is stirred and sonicated, (d1,d2) placed in molds, and (d3) dried; (d4) Dried slabs are (d5) calcined and sintered to produce (e1) nanofibrous highly porous ceramic slabs which are polished (e2) to the final shape.

Figure 2. SEM images of nanofibrous silica slab without ceramic binder after partial sintering at (a) 1000 ºC and (b) 1200 ºC.

Figure 3. (a) Volume and porosity changes of nanofibrous silica slabs with 5, 10, and 30 nm layer of Al_2O_3 or $MgAl_2O_4$ binder; Typical low-magnification SEM images of typical surface morphology of nanofibrous silica slabs with either binder after (b) calcination at 800 ºC and (c) partial sintering at 1200 ºC;

Figure 4. SEM images of nanofibrous silica slabs with (a,e) 30 nm binder layer after calcination at 800 ºC, and after sintering at 1200 ºC with (b,f) 5 nm, (c,g) 10 nm and (d,h) 30 nm of (a-d) Al_2O_3 or (e-h) $MgAl_2O_4$ ceramic binder, respectively.

Figure 5. SEM images of nanofibrous silica/ceramic layer structure after (a) calcination at 800 ºC and (b) partial sintering at 1200 ºC. The marked areas in (a) are: I – smeared binder layer, II – single silica nanofiber coated with binder layer, and III – a bundle of two or more nanofibers coated with binder layer; (c) artistic representation of typically observed features in nanofibrous silica/ceramic binder structures; (d,e) Damaged regions in sintered glass/ceramic nanofibers – (d) the arrow indicates the exposed silica core, and (e) reveals the binder layer thickness.

Figure 6. (a,b) SEM images of an individual broken sintered silica/Al_2O_3 twin fiber with a damaged binder layer. The brighter and darker areas on the fiber in (a) correspond to the binder layer and silica core, respectively; (c,d) Elemental map of Al (c) and Si (d) distribution, respectively, in the fiber (b); (e) EDS analysis of this fiber indicates a lower amount of Al_2O_3 than (f) the average for the whole sample. Carbon peak comes from the carbon support pad.

Figure 7. XRD patterns of nanofibrous silica slabs after (top) calcination at 800 ºC and (bottom) partial sintering at 1200 ºC with (a) 5 nm, (b) 10 nm, and (c) 30 nm layer of Al_2O_3 ceramic binder layer. * – amorphous silica phase; ▼– γ-alumina; ● – α-alumina.

Figure 8. X-Ray diffraction patterns of nanofibrous silica slabs after (top) calcination at 800 ºC and (bottom) partial sintering at 1200 ºC with (a) 5 nm, (b) 10 nm, and (c) 30 nm layer of $MgAl_2O_4$ (spinel) ceramic binder layer. * – amorphous silica phase; ▼ – spinel, respectively; ● –cristobalite; ♦ – sapphirine.

Figure 9. Representative stress-strain curves of nanofibrous silica slabs with Al_2O_3 or $MgAl_2O_4$ ceramic binder nanolayer in bending and compression after partial sintering at 1200 ºC of samples with (a) higher and (b) lower porosity.

Figure 10. Strength *vs* porosity trends in (a) bending and (b) compression for 800 ºC calcined (triangles) and 1200 ºC sintered (circles) nanofibrous glass/ceramic slabs with Al_2O_3 (grey symbols) or $MgAl_2O_4$ (red symbols) ceramic binder nanolayers. Dashed lines are to guide the reader's eye.

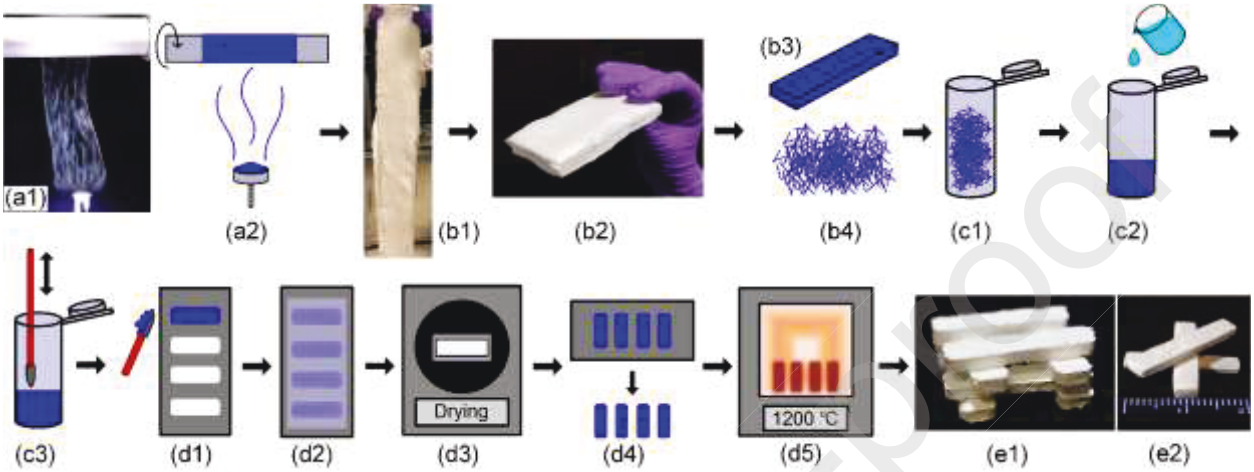

Fig. 1

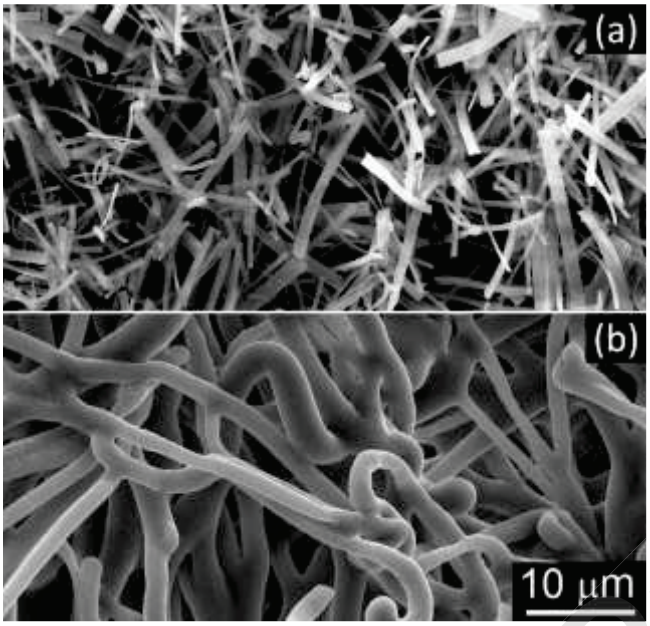

Fig. 2

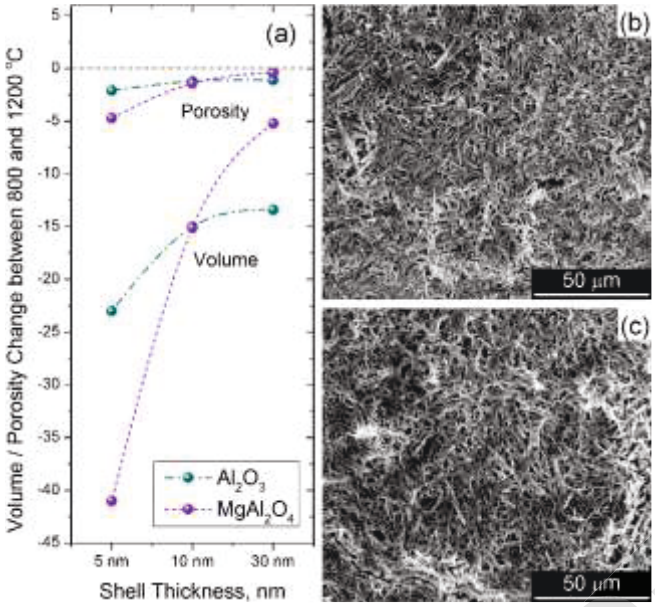

Fig. 3

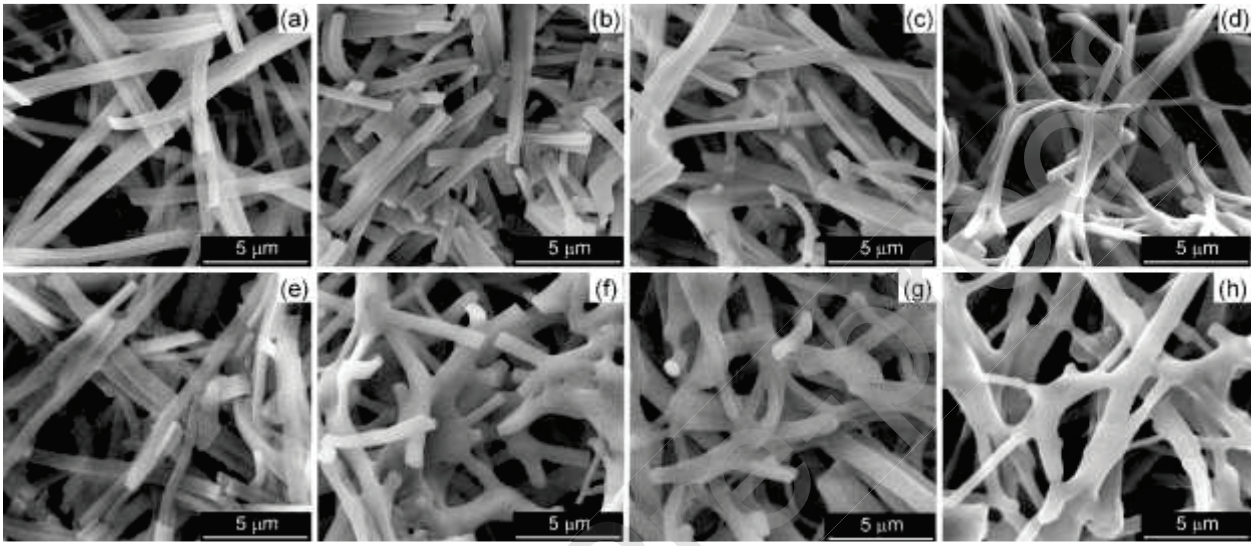

Fig. 4

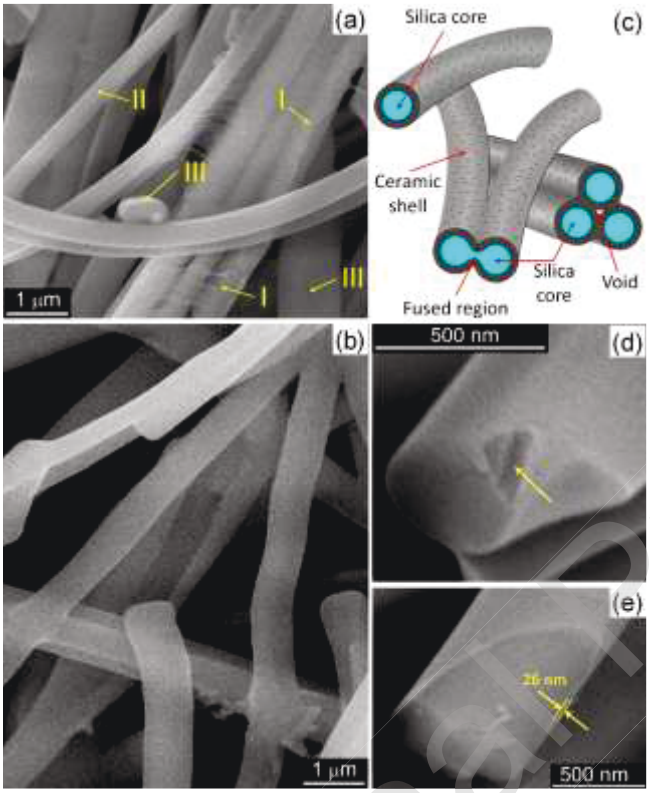

Fig. 5

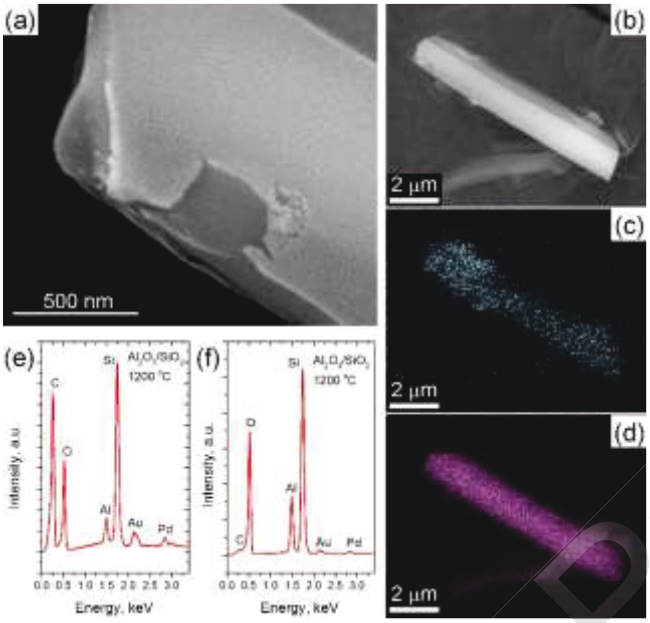

Fig. 6

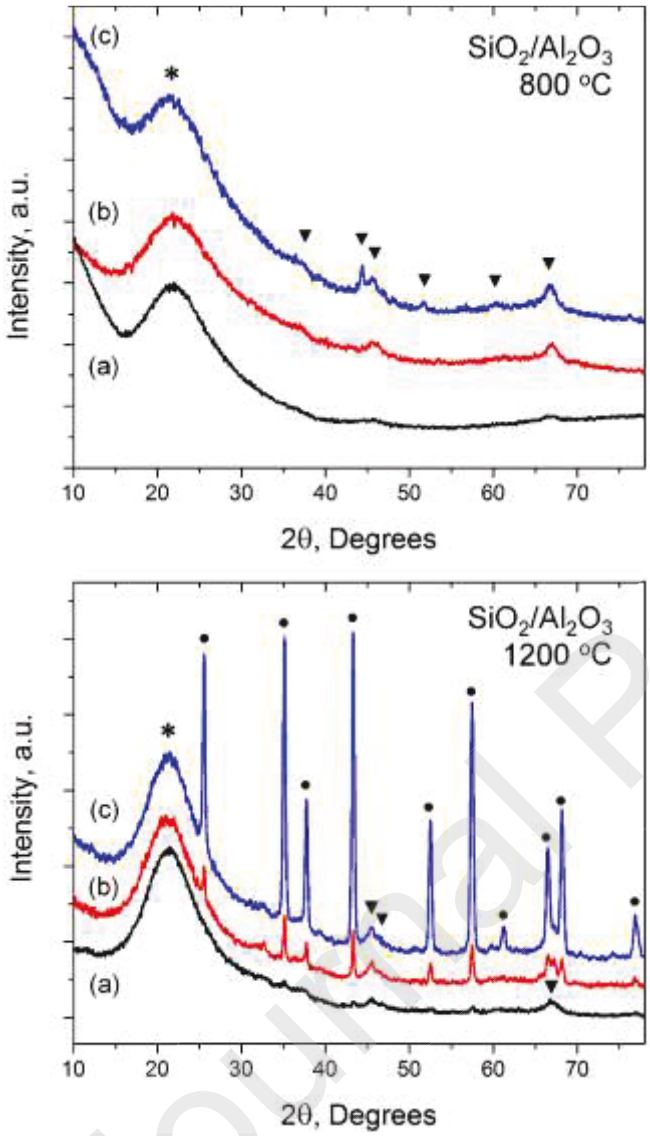

Fig. 7

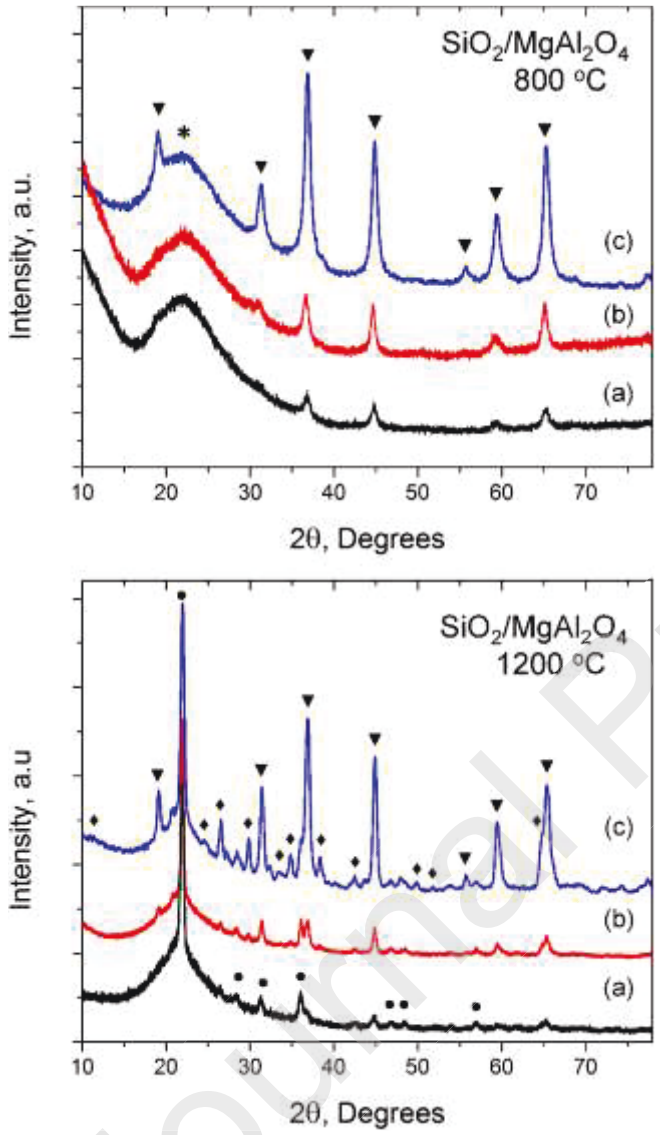

Fig. 8

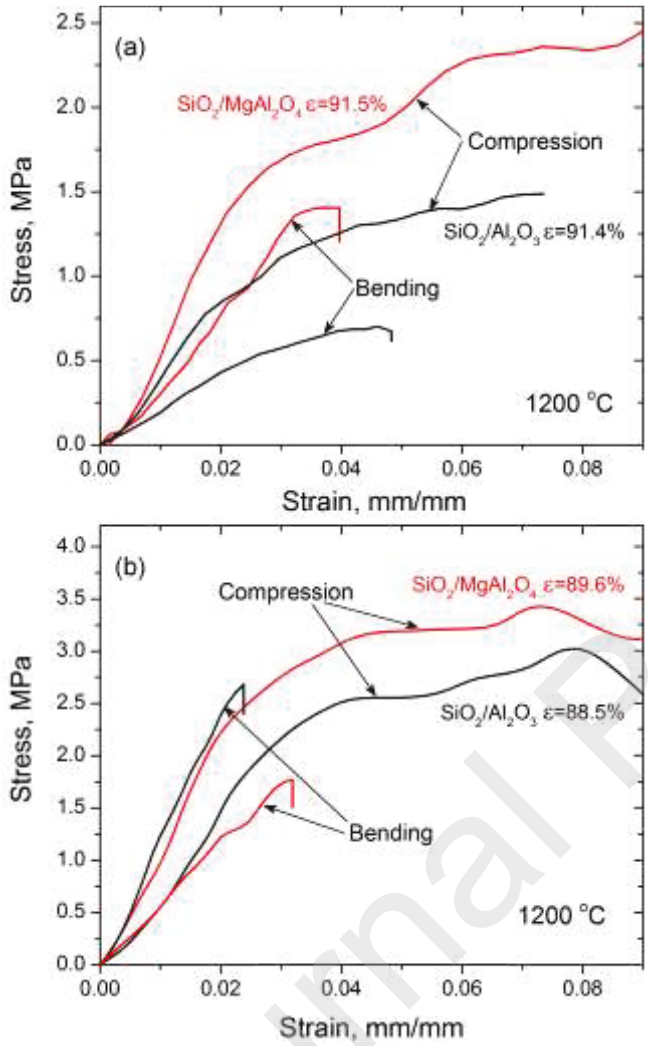

Fig. 9

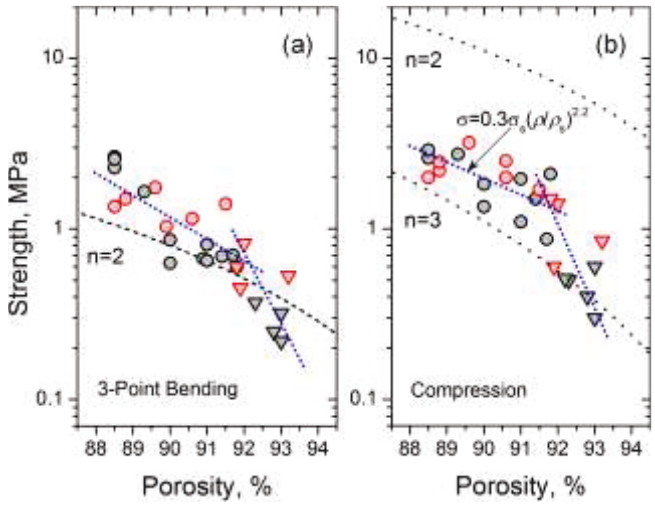

Fig. 10